Full-field Deformation Measurements in the Transmission Electron Microscope Using Digital Image Correlation and Particle Tracking

Y. Zhang[1], L. Feng[2], S. Dillon[3], J. Lambros[1,*]

[1]Department of Aerospace Engineering, University of Illinois at Urbana-Champaign, Urbana IL 61801

[2]School of Chemical Engineering and Technology, Sun Yat-sen University,

Zhuhai, Guangdong, China, 519082

[3]Department of Materials Science and Engineering, University of California Irvine, Irvine CA 92585

* corresponding author: lambros@illinois.edu; Tel: 217-333-2242; Fax: 217-244-7020.

Abstract

Determining displacement and/or strain fields at the nanoscale during material deformation can be instrumental in developing a multiscale understanding of material response. Full-field quantitative kinematic measurements based on transmission electron microscopy (TEM) are lagging behind other microscopy techniques. Here, we develop an experimental approach combining digital image correlation (DIC) and particle tracking (PT) for characterizing *in situ* microscale deformation of amorphous SiO_2 in the TEM. Gold nanoparticles deposited on SiO_2 provide both the speckle pattern required by DIC when averaged over a subset region and target particles for PT. To demonstrate and validate the feasibility of using DIC and PT in the TEM, micron sized SiO_2 beam samples are machined using a focused ion beam (FIB) and loaded in the TEM via indentation. DIC and PT are then applied to measure *in situ* displacements from a sequence of TEM images taken during loading and creep of the beam. Results of the two measurement methods agree well with each other and with the applied displacement measurements, thus demonstrating their effectiveness in determining local displacements from TEM experiments. Sources of noise resulting from sample drift and image intensity variations are discussed.

Keywords: Digital Image Correlation; Particle tracking; *In situ* deformation; Transmission Electron Microscopy

Materials Characterization

1. Introduction

In situ mechanical testing in the transmission electron microscope (TEM) has been used extensively for several decades to characterize a variety of materials such as: single-crystals [1,2], metallic glasses [3,4], thin films [5], nanowires [6] and complex materials such as high-entropy alloys (HEA) [7]. In earlier studies the TEM was employed primarily for imaging and was used to identify key deformation mechanisms, [8]. *In situ* mechanical testing within the TEM has progressively become more quantitative through the development of MEMS-based testing and commercial nanomechanical testers [9,10]. Such testing enables both qualitative observation of micro/nanoscale deformation events and quantitative measurement of material response measured using a variety of microscale loading configurations such as dog-bone tensile tests [11], cantilever bending [7], pillar compression [11], notched fracture loading [12], or fatigue [13]. An important aspect of material response that can be obtained in these experiments is the quantitative understanding of strain localization at the microscale, relevant not only to failure phenomena (e.g., fracture, fatigue, shear banding) which are inherently localization driven, but also to macroscopically homogeneous deformations that may be highly heterogeneous microscopically as a result of boundaries and interfaces, e.g., twin, grain, or phase boundaries.

Microscale and nanoscale investigation of material response can provide insight into mechanisms that influence macroscale response [14]. Interface properties, which are needed for predicting mesoscale response of polycrystalline materials, i.e. at a length scale at which interaction between two or more grains takes place, have been of particular interest in *in situ* TEM studies of strain localization [7,12,15]. For example, Zou et al. [7] illustrated that varying fracture toughness and strength on single-crystal and bi-crystal $Nb_{25}Mo_{25}Ta_{25}W_{25}$ can be attributed to grain boundary segregation. More recently, Feng et al. [12] studied the influence of grain boundary

complexion and dopant chemistry on the fracture response of alumina. In Reference [12] grain boundary toughness at the TEM length scale was determined from *in situ* experiments on micro-cantilever beams with a notch aligned with the grain boundary while measuring applied far-field load-displacement response using a TEM loading stage. Mechanical response along the grain boundary was then obtained by using finite element simulations. Although measured *in situ*, the approach only provides far-field load-displacement data. When dealing with problems that may involve significant deformation localization, such as for example near a notch-tip, full-field displacement measurements in the TEM would provide a significant wealth of information beyond the applied loading conditions.

Digital image correlation (DIC) is a popular non-contact optical method developed in the 1980s for displacement and strain field measurements [16,17]. Since its inception, DIC has been widely applied to characterizing macroscale material response [18,19] and more recently has been extended for use in mesoscale studies using optical microscopy [20,21], microscale studies using scanning electron microscopy (SEM) [22–28] scanning tunneling microscopy (STM) [29], atomic force microscopy (AFM) [30]. To our knowledge, there has been one recent study that employed DIC measurements in a TEM environment [31]. In the pioneering work of [31] the inherent texture of an amorphous Si material was used as the identifying features for DIC correlation and deformation was introduced by electrochemical lithiation rather than mechanical loading (since studying high-capacity battery electrode applications was a motivating interest there). In the present effort we will generalize the approach of [31] by adding an externally deposited speckle pattern for DIC and we will use the developed methodology in a variety of mechanical loading situations, thus making DIC in the TEM amenable for use more broadly in other materials/loadings. Conventional DIC cannot capture the kinematical discontinuity of plastic localization in shear

bands and slip bands well. Valle et al. recently applied high resolution Heaviside-DIC to characterize discontinuous plastic deformation and strain localization [32,33]. However, TEM can directly image dislocation motion, slip bands, and shear bands potentially providing the ability to pair qualitative imaging results with quantitative DIC measurements.

An alternative to DIC *in situ*, and to some extent full-field, displacement measurement approach is to track the positions of individual particles as they continuously move during sample deformation, in what is commonly known as particle tracking (PT). Relative to DIC, PT is somewhat limited in obtaining sub-pixel resolution, and only measures displacements rather than displacements and strain. PT is, however, less sensitive than DIC to coherent scattering, common in crystalline materials. Since strains often influence the diffraction condition of crystalline materials, the intensities of DIC subsets in those materials can potentially vary throughout the experiment. This effect likely accounts for the limited application of DIC to in situ TEM-based mechanical testing data.

Full-field measurements at the microscale and nanoscale resulting from *in situ* TEM experiments would open a new avenue of metrology for materials assessment, especially in regions of high localization such as grain boundaries, crack tips, shear bands in crystals and metallic glasses. In this paper, we aim to develop methods for *in situ* full-field displacement measurement in the TEM. By generating and tracking appropriate speckle patterns on a sample we can apply DIC and PT on images acquired during *in situ* loading and deformation experiments. Here we will discuss the methodology of implementing these techniques in the TEM including the application of a speckle pattern, the limitations of the DIC and PT correlation procedures in the TEM, and noise and image drift inaccuracies present in the TEM. Results of DIC and PT will be compared to evaluate their effectiveness and their range of applicability.

2. Experimental Methods: Specimen Preparation and Loading

2.1 Material

Commercial thermally grown 1 μm thick amorphous SiO_2 on Si samples (UniversityWafer, Inc.) were used for these experiments. This material was selected as a demonstration material because of its wide availability, low cost and ease of preparation. The approach should, however, be easily adaptable to a host of other amorphous materials for which similar specimen preparation is possible. A small piece of the SiO_2-coated wafer with in-plane dimensions approximately 3 mm by 2 mm was cleaved using a diamond scribe. The piece was then polished on an Allied Multiprep polishing apparatus using 9, 3 and 1 μm aluminum oxide lapping films in sequence. The sample was polished at 45° on the Si side until the edge of the polished side was only a few microns thick, thus forming a wedge shape. The main goal of this polishing procedure was decreasing the sample thickness prior to focused ion beam (FIB) milling (described in section 2.3). Note that even though the sample used here has a smooth surface on the polished side, there is no strict requirement on the specimen surface roughness values. Prior to FIB milling, a surface speckle pattern is deposited to serve in the dual role of DIC speckles and PT markers.

2.2 Pattern Deposition for Image Correlation and Particle Tracking

DIC requires the existence of a random speckle pattern which will be used for tracking as deformation progresses (more details on the DIC method itself are given in the next section). One particular challenge when applying DIC to the microscale, especially in the SEM, STM and AFM environments, is the generation of such a random speckle pattern on the sample. In the past various methods of generating DIC patterns have been developed, including chemical etching [34], electron beam lithography [35], scratching [36] and nanoparticle deposition [37–39]. Of particular relevance here is the work of Soo et al. [40] who developed a nanodot pattern for DIC by thermal

de-wetting of a deposited thin film. A similar method is employed herein and is discussed in detail below.

The DIC pattern was deposited prior to FIB milling in order to avoid the evolution of thermally induced residual strains in the final sample geometry during pattern formation. A method, described below, was developed to relax residual stresses prior to the final stages of FIB milling. One disadvantage of this approach is the possibility of damaging the pattern itself during the FIB process.

The pattern must possess sufficient contrast difference from the substrate material, in this case SiO_2, to be clearly identified in the resulting image. Furthermore, the speckle pattern must remain attached to the sample surface, whose deformation it must conform to, but not affect, which is verified here through numerical simulations. For the case of SiO_2, gold was chosen as a suitable material to form the surface speckle pattern because of its high density. In order to generate speckles on the sample surface, a uniform gold layer was first deposited on the surface of SiO_2 using an e-beam evaporator. Solid-state de-wetting occurs during thermal annealing in order to minimize surface energy, resulting in individual gold nanoparticles randomly distributed on the surface [41]. The number density and size of these nanoparticles is sensitive to the annealing conditions [42]. A 5 nm thick film was deposited and then annealed at 630°C for 1 hour. The process produces particles with a mean Feret diameter of 41.6 nm. An SEM image of the particles resulting after this annealing process is shown in Fig. 1. The specific thickness, temperature and time were arrived upon using an experimental factorial design study in which each of these three parameters were varied independently to arrive at the desired pattern shown in Fig. 1. Note that in the event that, for example, one would want to use a different, say higher, magnification in the TEM, a finer pattern would be needed, which would mean that one or more of these annealing

process parameters would need to be changed accordingly. For DIC, a minimum of 3 to 5 speckles should typically occupy each side of the area to be correlated, i.e. subset size.

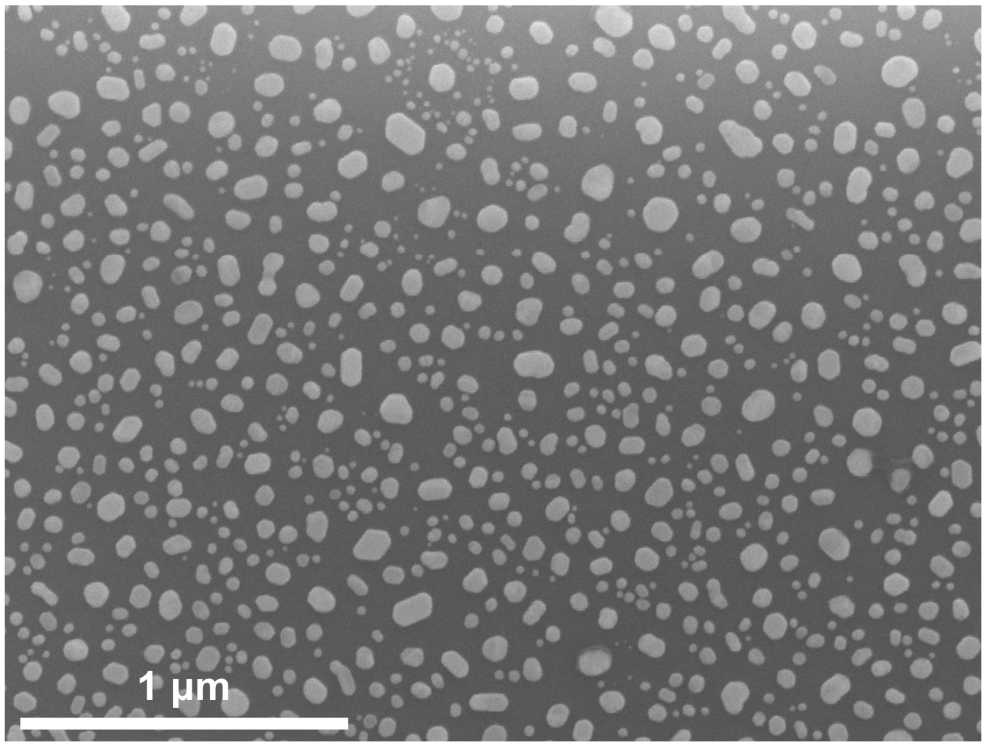

Fig. 1 SEM image of gold nanoparticles formed on an SiO_2 substrate via thermally induced de-wetting of a gold film.

2.3 Focused Ion Beam Milling

After growing the desired pattern on the Si/SiO_2 specimen, it was then mounted onto a sample holder for the Bruker PI95 Picoindenter and placed in the FIB. The sample is FIB milled on the Picoindenter sample mount to ensure good axial alignment with the indenter. A beam with built-in ends on both sides was prepared to enable beam bending type experiments with loading at the center of the span. The beam dimensions were approximately length L = 20 μm, width w = 2 μm and thickness t = 0.45 μm. Fig. 2 depicts the nominal configuration of the beam and specimen. Samples were milled using a 30 keV accelerating voltage and currents between 7 nA and 50 pA.

Because of the existence of residual stress, buckling of the specimen occurs while reducing the thickness of the beam to less than 0.5 μm. Fig. 3 shows an example of a buckled beam. Since the aim of this work is to develop the DIC/PT for TEM application rather than study the Si/SiO_2 wafer specifically, we followed a procedure to reduce residual stresses before completely thinning down the beam in the FIB. To this end, the sample was irradiated by 200 keV electrons for 20 minutes in the TEM after the sample thickness was reduced to around 1.3 μm, a thickness, which is thin enough to allow the TEM electron beam to penetrate through the sample but also thick enough to suppress the spontaneous buckling of the machined beam in the FIB. It is known that irradiating amorphous SiO_2 in a TEM causes stress relaxation [43,44], a fact which is exploited to reduce the residual stresses causing the buckling seen in Fig. 3. The sample, now free of large residual stresses, was then returned to the FIB and milled to a final thickness of 0.45 μm. Ion beam images of a finished sample are shown in Fig. 4.

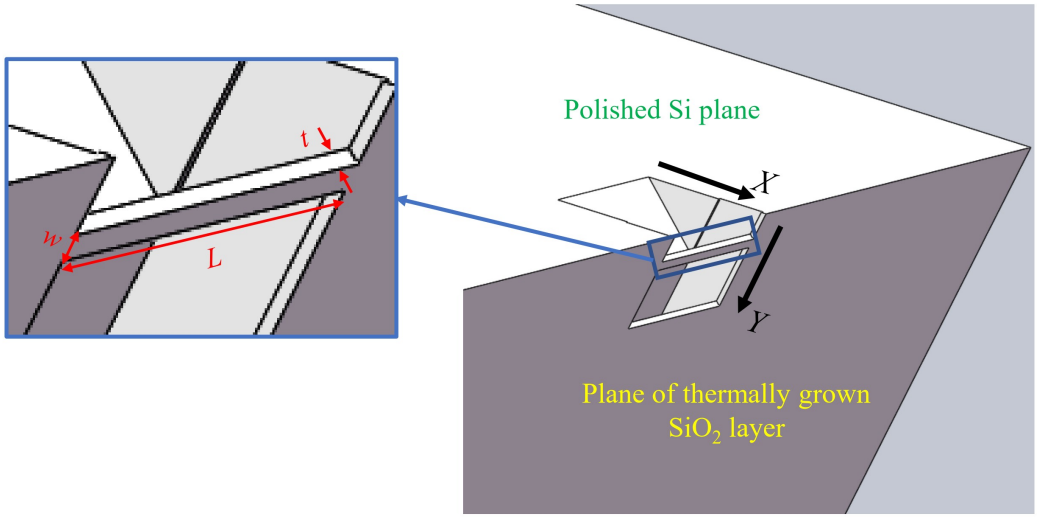

Fig. 2 Configuration of the microbeam milled in the FIB; *X* and *Y* indicate beam thickness and width directions, respectively. The speckle pattern is applied on the surface that is depicted as the darkest grey level in the image.

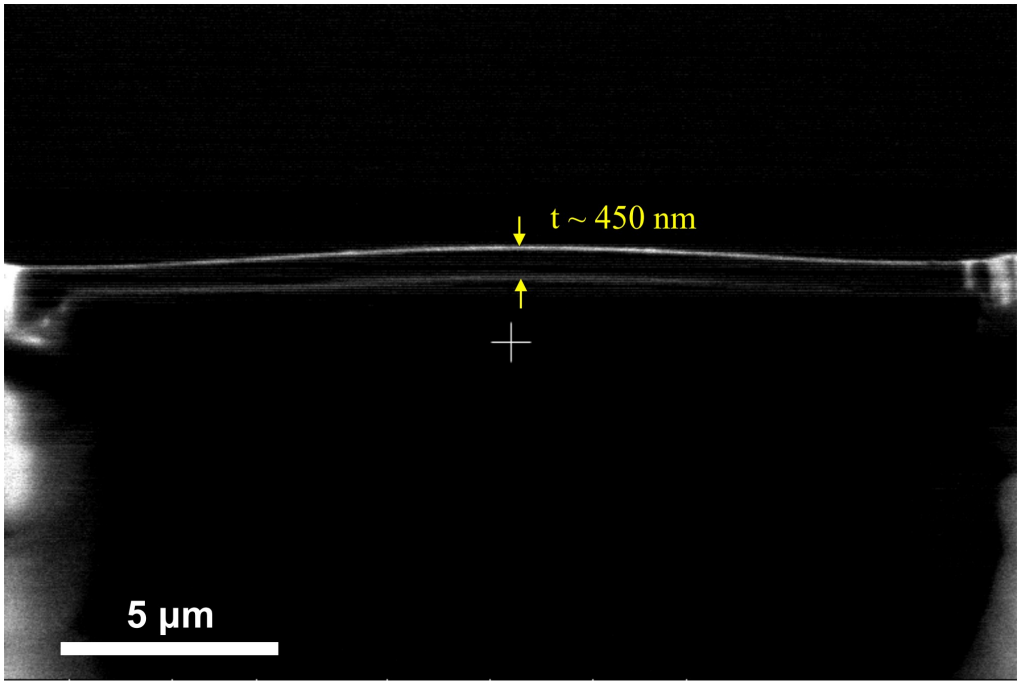

Fig. 3 Beam buckling observed during FIB milling, at thickness < 500 nm, resulting from residual stresses.

2.4 *In situ* TEM loading experiments

In situ experiments were performed using a Bruker PI 95 PicoIndenter. Loading was applied at the midspan of the beam by indentation contact of a 1 µm diameter round circular flat diamond punch using load control. *In situ* images were taken at 2048 pixel x 2048 pixel resolution, using an Gatan UltraScan 1000 CCD camera at 0.4 s exposure time in a JEOL-2100 TEM. A series of baseline test images were also obtained using a Hitachi H9500 equipped with an Orius 200 camera, in order to compare results from different microscope and camera configurations. At an indicated 5000x magnification, the field-of-view corresponds to a ~ 4 µm x 2 µm region near the loading point, as seen in Fig. 5. Recall that the entire beam length is approximately 20 µm, with the relative field of view as seen in the box shown in Fig. 4a. Note that since imaging is in transmission, two options for positioning the sample in the TEM exist: with the patterned surface facing the incident

electron beam, or with the patterned surface away from the incident electrons. To investigate whether sample placement can affect the imaging of gold particles, we performed experiments in both configurations. Under the microscope settings described above, there was no significant difference observed in image quality or correlation ability between either placement at the magnifications used. All experiments described are performed with the speckle particle patterns facing the incident electron beam in the TEM.

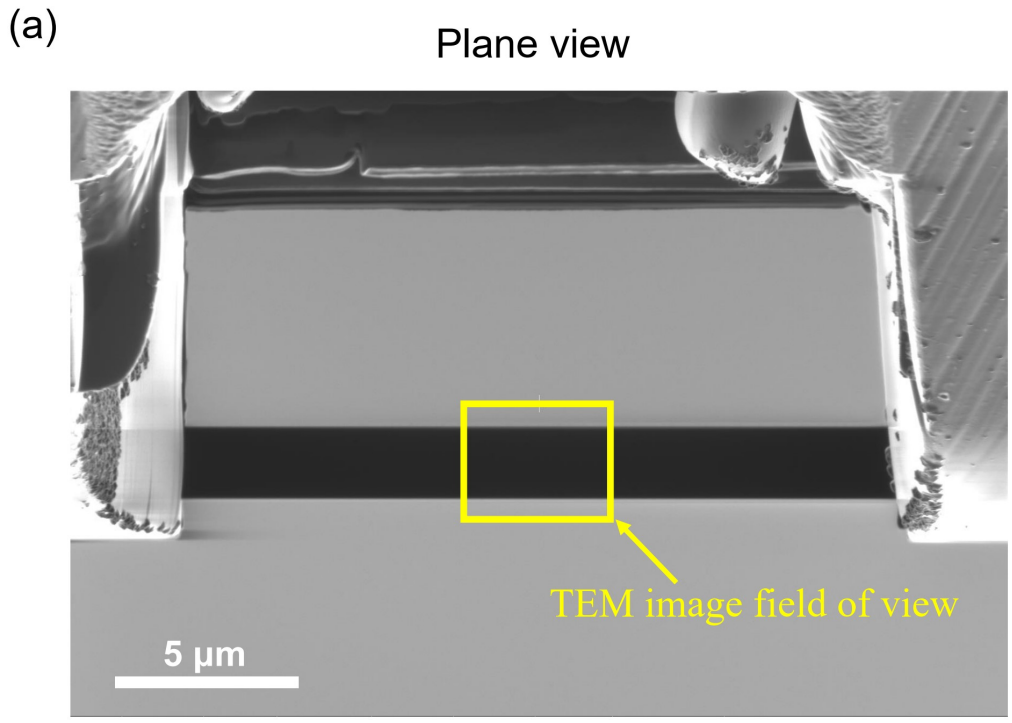

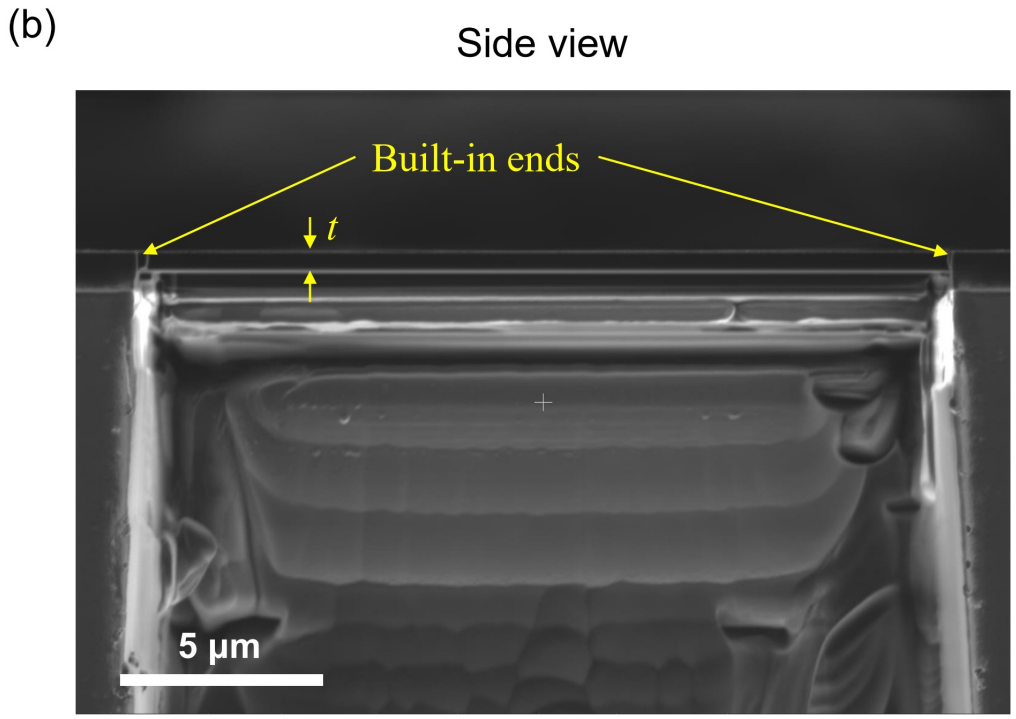

Fig. 4 FIB secondary electron images taken using the ion beam illustrating (a) the beam length and width, and (b) the beam thickness.

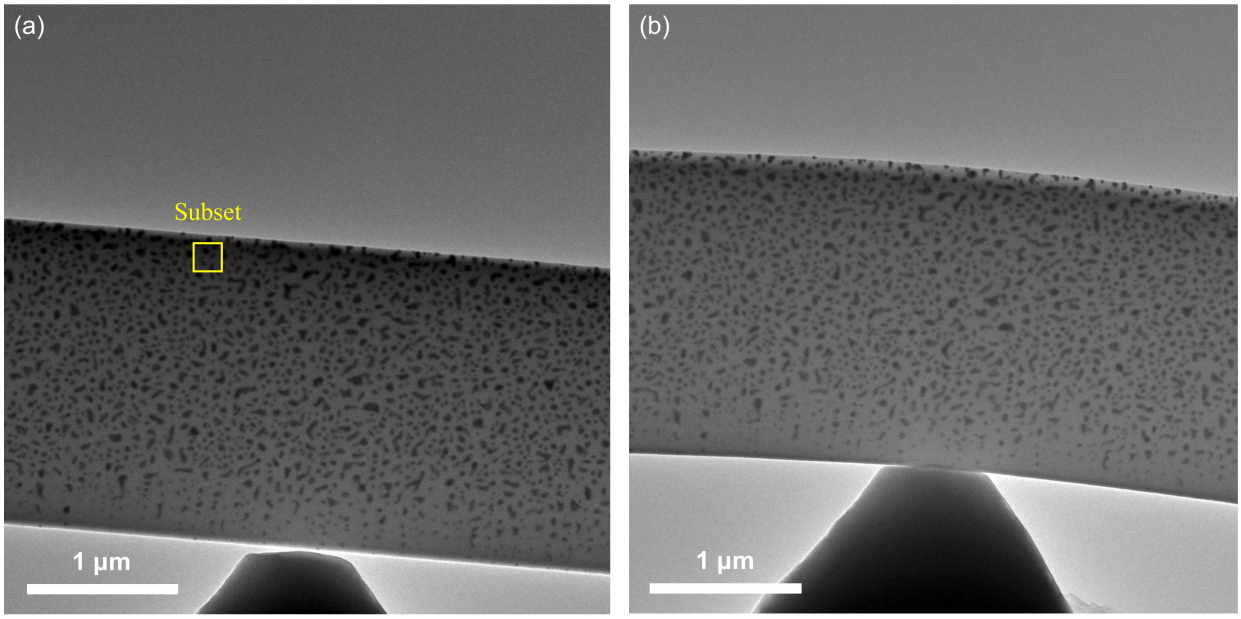

Fig. 5 In-situ TEM images acquired at (a) t = 0s (undeformed); (b) t = 296s (deformed).

Since SiO_2 exhibits creep behavior under electron beam irradiation [43,44], the beam sample should undergo continuous deformation under fixed loading during continuous electron imaging. This type of creep loading is suitable for qualifying the displacement and strain measuring capabilities of DIC and PT. A ramp-step loading procedure, shown in Fig. 6a, was used as the control input to the indenter force profile in order to investigate the practicality of tracking deformation resulting both from ramp loading, over 23 s, and creep, between 23 s and 300 s. Fig. 6b shows the corresponding displacement at the load point as measured from the loading actuator, i.e., far-field measurement, and from DIC and PT at the loading point; see section 4.3 for details. In addition to undeformed images before loading, three images were manually taken during the ramp loading stage, at approximately constant time intervals, and 11 images were manually taken during the constant load stage, also at approximately constant intervals, for a total of 14 images during each experiment. Automatic time stamps in each image allow precise synchronization to the load profile shown in Fig. 6a which is recorded on the same time base.

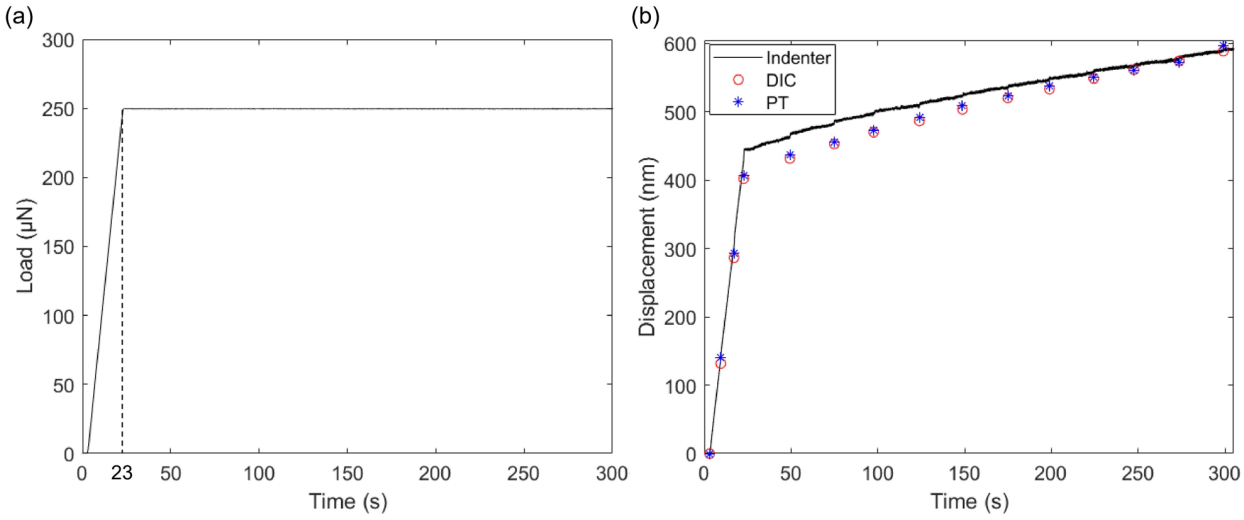

Fig. 6 (a) Ramp-step load control history used as the control input for the indenter. (b) Resulting load point displacement as measured by the loading actuator, along with DIC and PT measurements at locations within ≈ 300 nm of the loading point.

3. DIC and PT analysis

3.1 Digital image correlation (DIC)

Two-dimensional DIC analysis was performed using VIC-2D [45], a commercial software suite from Correlated Solutions. Although DIC is a well-established technique that has been used extensively over the past several decades for nano/micro/macroscale studies, in the interest of completeness we will present here a brief description of how the method works. The reader is referred to reference [45] for more details. Consider the schematic in Fig. 7 which illustrates the deformation of a subset on the specimen surface represented by a square region, the undeformed configuration, that undergoes an affine deformation into a parallelogram form, the deformed configuration. Assuming a homogeneous deformation within the subset, the coordinates of any point in the deformed subset configuration (e.g., point q') can be written as a function of the deformation of the center point p as:

$$x'_{q'} = x_q + u_p + \frac{\partial u_p}{\partial x}\Delta x_q + \frac{\partial u_p}{\partial y}\Delta y_q \tag{1}$$

$$y'_{q'} = y_q + v_p + \frac{\partial v_p}{\partial y}\Delta y_q + \frac{\partial v_p}{\partial x}\Delta x_q, \tag{2}$$

where u_p and v_p are displacement components of point p along the x and y directions respectively and $\Delta x_q = x_q - x_p$ and $\Delta y_q = y_q - y_p$. Assuming that the surface speckle pattern intensity distribution of the sample between the undeformed and deformed configuration does not change but simply moves in a locally affine fashion, we can express the intensity distributions by discrete functions $F(x,y)$ and $G(x',y')$. DIC performs an inverse analysis of Eqn. (1) and (2) to determine the unknown vector of displacement and displacement gradients at p, i.e. $\overrightarrow{V_p} = \left[u_{x_p} \;\; u_{y_p} \;\; \frac{\partial u_p}{\partial x} \;\; \frac{\partial u_p}{\partial y}\right.$

$\frac{\partial v_p}{\partial x}$ $\frac{\partial v_p}{\partial y}\Big]$, by minimizing the difference in intensity between the deformed and undeformed subset using a given metric. In the event that there are global intensity changes (i.e., changes in the average value), a common occurrence in many TEM systems, the zero-mean normalized sum of squared difference (ZNSSD), which can eliminate influence from scaling and offset in global intensity variation can be used in the minimization:

$$C_{ZNSSD} = \sum \left[\left(\frac{\sum (F_i - \frac{\sum F}{n})(G_i - \frac{\sum G}{n})}{\sum (G_i - \frac{\sum G}{n})^2} G_i - \frac{\sum G}{n} \frac{\sum (F_i - \frac{\sum F}{n})(G_i - \frac{\sum G}{n})}{\sum (G_i - \frac{\sum G}{n})^2} \right) - F_i + \frac{\sum F}{n} \right]^2 \quad (4)$$

where n is the number of pixels in the area of interest .

Important user-selected parameters in this process are the subset size to be used in the correlation and the distance between subsets, or correlation interval, which will fix the density of measurement points since each correlation result will be assigned to the center point of a subset, p. For all correlations performed herein a subset size of 95 pixels by 95 pixels (201 nm by 201 nm), shown as the square in Fig. 5a, was used. Typically, we use half the subset size as the distance between correlation points. Due to the long aspect ratio of our structure, a distance of 20 pixels (42 nm) between subsets was used to increase the data acquisition frequency. More details on how these parameters were selected are given in the supplementary material.

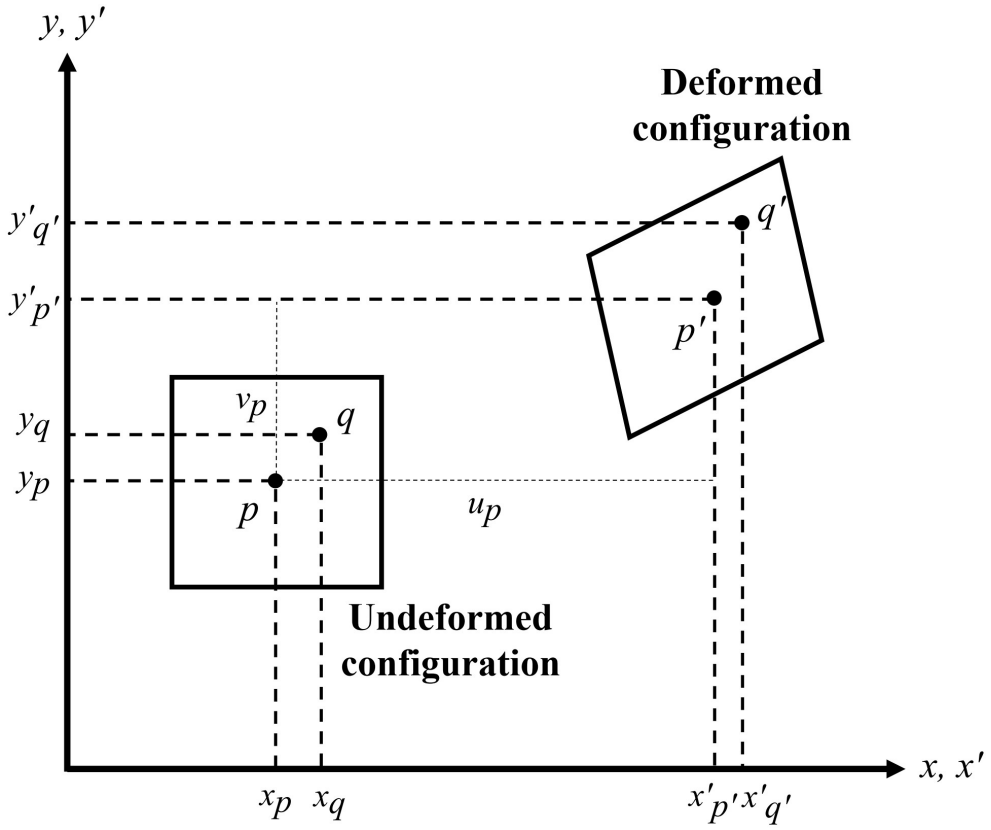

Fig. 7 Schematic of a body under planar deformation.

3.2 Particle tracking (PT)

The particle tracking analysis was carried out using the Trackmate module [46] in the open-source Fiji ImageJ software [47]. The Trackmate module gives displacement information by first identifying particles in each image according to the manually-assigned estimated particle diameter, and then linking the tracked particles in each image restricted by the linking maximum distance specified by the user. Coordinate values for the center of mass of each particle are then extracted representing particle location for each image of a sequence of images. Unlike DIC where raw uncompressed images were used to preserve sub-pixel accuracy, some preprocessing was applied to the raw TEM images by inverting their intensity maps in order to obtain bright dots on a dark

background, as shown in Fig. 8. Brightness and contrast were also adjusted accordingly to highlight particles for ease of tracking.

Particle detection was carried out using the Laplacian of Gaussian (LoG) detector algorithm applied to the source image [48]. Particle position is determined by searching for local maxima of the filtered image intensity. The LoG result is calculated by summing second-order spatial derivatives of a Gaussian-filtered image, with a normalized scale. Note that the standard deviation of the Gaussian filter: $\sigma = \frac{d}{2\sqrt{n}}$, is tuned by the particle diameter d that is an input in the algorithm, and n is the dimensionality of the source image (n = 2 for 2D in this work).

We utilized an input value d =36 pixels. The detected particles are highlighted by magenta circles in Fig. 8. The specified value of d will affect the determined position of the particle. In this work, ±5 pixels (10.6 nm) of variation in d will result in a maximum deviation ~0.27 pixels (0.57 nm) in the determined positions of individual particles, which reveals the systematic bias but low sensitivity in particle detection.

Particle linking was performed using a linear assignment problem (LAP) tracker developed by Jaqaman and colleagues [49]. The fundamental idea of LAP is assembling a cost matrix that contains cost values (defined as the square of linking distance, D^2) of all possible linking assignments (i.e. each particle in a frame can be assigned to link to any other particles in the next frame, or not to link). The reader is referred to reference [49] for more details. Actual assignments of LAP are derived by solving the matrix for minimal total cost via the Munkres & Kuhn algorithm [50]. Note that in Trackmate, the maximum linking distance, D_{max}, is manually input by the user. The link is forbidden the linking distance $D > D_{max}$. In this work, we set the maximum linking distance D_{max}= 78 pixels, according to the displacement of the diamond punch.

The results of the application of Trackmate to a series of images are shown as selected trajectories in Fig. 8, details will be discussed in Section 4. It should be noted that the PT algorithm is more effective when the linking distance between particle positions in subsequent images is small relative to the spacing of particles in the speckle pattern [51]. Data obtained during *in situ* deformation was collected at relatively long-time intervals in order to collect images with reproducible intensity distributions for DIC analysis. Data collection was not optimized for PT that would likely benefit from higher temporal resolution, which would result in smaller linking distances between images.

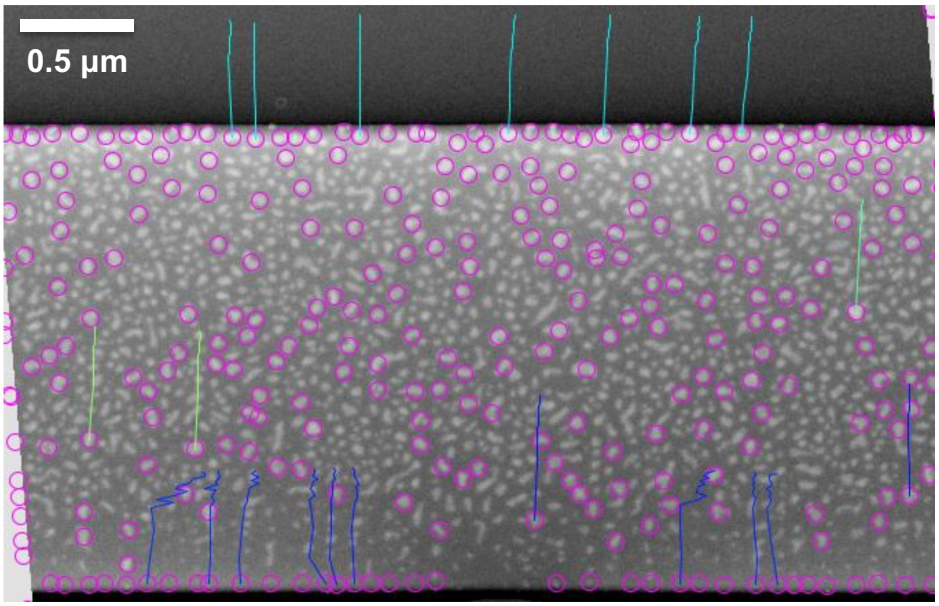

Fig. 8 Example pre-processing of raw TEM image for PT. The magenta circles highlight identified particles and the lines depict specific tracks identified.

4. Results and Discussion

4.1 DIC noise analysis

Before obtaining DIC results that can be compared to the PT results in Fig. 8, we are interested in estimating noise levels for DIC in the TEM. Note that PT can be more robust when larger motions are present, although it requires frequent image acquisition. DIC produces better sub-pixel measurement resolution than PT, and can also be applied effectively at large deformations by performing incremental correlation. Primary sources of noise in DIC applied to TEM data may differ from those associated with optical experiments. Possible sources of additional error in the TEM include: damage to the pattern by the electron beam incident on the sample, thermal drift and temperature fluctuations at the nanometer length scale, variability in camera imaging including any intensity scaling performed by the TEM camera, vibratory noise, and electron beam intensity variation, among others [31]. In order to quantify these effects and determine a baseline for an acceptable signal-to-noise ratio for use of DIC in a TEM, images from two different microscopes, a JEOL 2100 TEM with a Gatan UltraScan 1000 camera and a Hitachi H9500 TEM with a Gatan Orius SC200 camera, were acquired for baseline tests and analyzed in VIC-2D to evaluate noise level.

Correlating baseline images, i.e., a series of undeformed state images taken before loading, is a way of obtaining a measure of the inherent noise in a particular DIC setup. The quiver plot in Fig. 9a visualizes both the horizontal and vertical displacement components, and provides an example of the raw VIC-2D DIC results for a baseline correlation in the JEOL 2100. If only random noise were present, then randomly oriented quivers would be anticipated on the plot. As highlighted by the inset of Fig. 9a, rigid motion clearly occurs due to sample drift. This is in addition to possible underlying random noise which is likely being overwhelmed by image drift.

Such image drift commonly results from thermal noise or hysteresis resulting from motion of the sample stage.

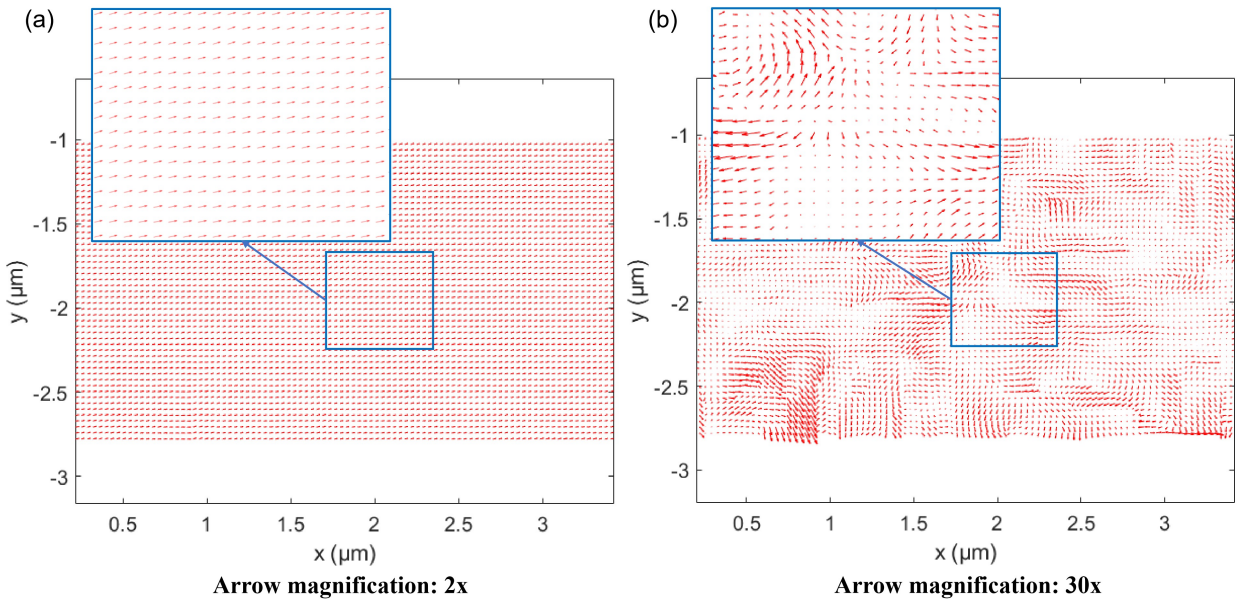

Fig. 9 Quiver plots from baseline experiments highlighting (a) image drift in the JEOL 2100 and (b) the noise level after subtracting fitted average rigid displacements.

To evaluate noise level versus image drift, we start by assuming that most of the image drift consists of rigid translations which can be computed by calculating the average vertical and horizontal displacements. Fig. 10 shows the average horizontal and vertical displacement illustrating image drift in both the JEOL and Hitachi microscopes. The average results are shown as circle or triangle symbols and errors bars shown on each symbol represent one standard deviation. The actual values of average displacement, with one standard deviation as scatter, for the JEOL case are shown in Table 1 as u_{DIC} *and* v_{DIC}. The evolution of image drift in each microscope can be seen as the evolution with image number, 6 in each case. Fig. 10c shows the same data combined as the total displacement magnitude ($\sqrt{u^2 + v^2}$) for both cases as a function

of image acquisition time. Although the amounts and directions of drift are different in each case, the trends are similar. By fitting image acquisition time and total displacement from DIC, an average linear drift speed can be calculated, 7.88×10^{-5} μm/s in the JEOL 2100 and 3.17×10^{-5} μm/s in the Hitachi H9500. Note that the rate and direction of drift is sensitive to hysteresis and environmental conditions at the time of acquisition. For the JEOL 2100, the amount of drift was ~ 0.03 nm during the 0.4 s exposure time, which is much smaller than the pixel size of ~ 2 nm. This indicates that image drift should not affect the intensity distributions used in the DIC analysis.

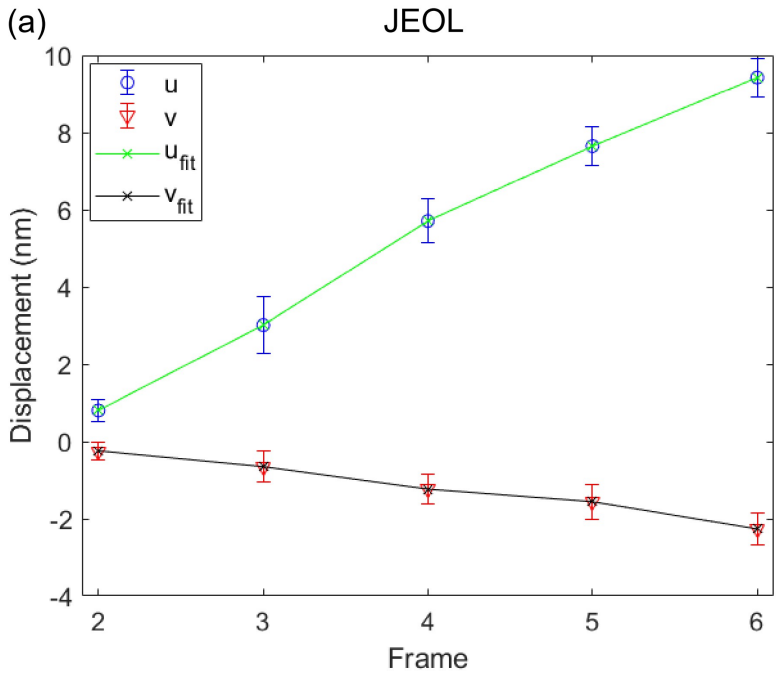

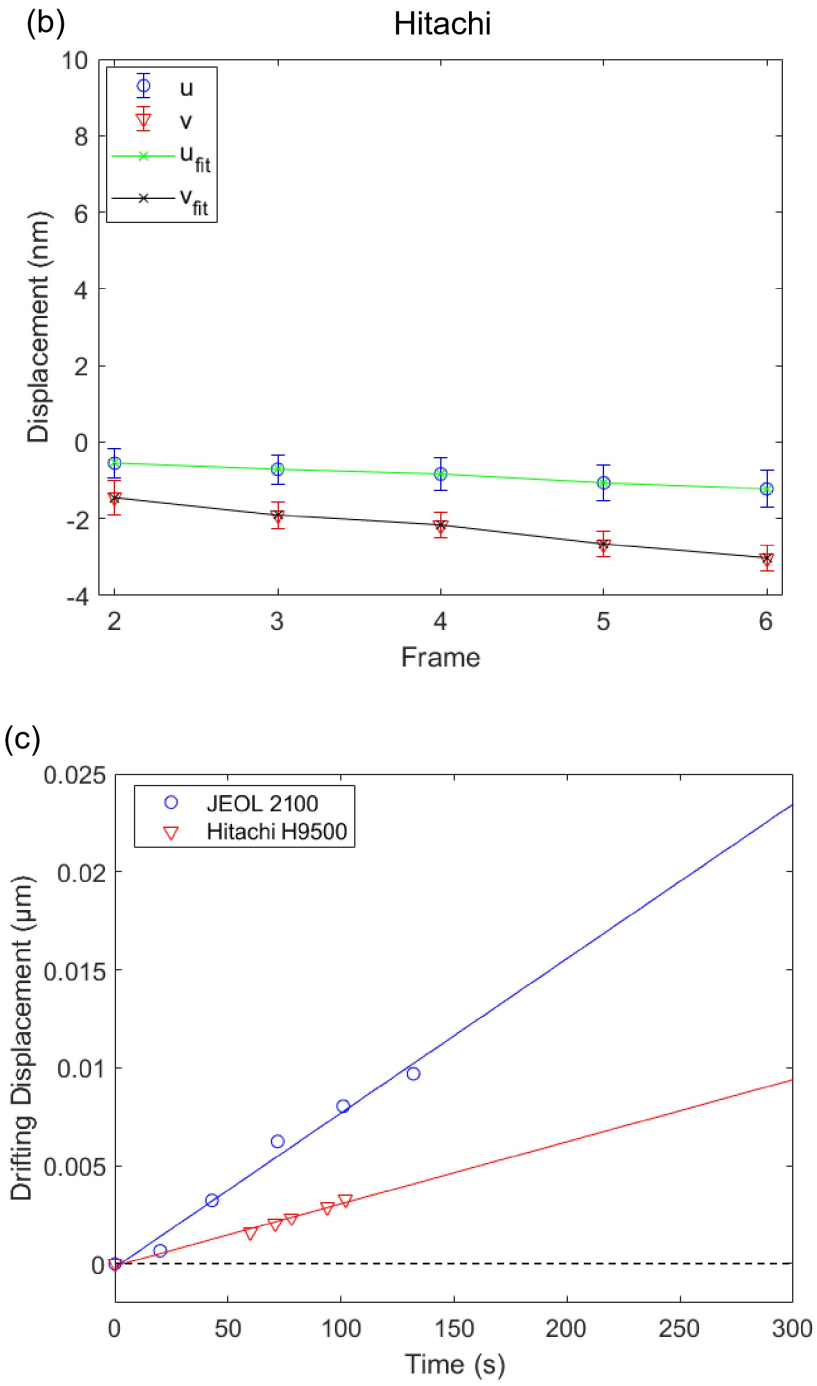

Fig. 10 DIC measurement of average displacement versus frame number for (a) the JEOL 2100 and (b) the Hitachi H9500. The average time between frames is 26 s and 21 s in (a) and (b), respectively. (c) shows average displacements resulting from drift of two baseline tests.

	DIC						PT	
frame	u_{DIC} (nm)	A_1 (mrad)	A_2 (nm)	v_{DIC} (nm)	B_1 (mrad)	B_2 (nm)	u_{PT} (nm)	v_{PT} (nm)
1 (ref)	0	0	0	0	0	0	0	0
2	0.80±0.29	-0.091	0.97	-0.25±0.24	0.008	-0.26	1.56±0.92	-0.39±0.87
3	3.02±0.72	-0.151	3.30	-0.66±0.39	-0.017	-0.62	3.56±0.11	-0.85±0.98
4	5.71±0.57	0.020	5.67	-1.24±0.39	0.004	-1.24	5.74±1.03	-1.19±1.00
5	7.65±0.50	0.054	7.55	-1.56±0.44	0.045	-1.64	7.63±1.15	-1.49±0.92
6	9.43±0.49	0.051	9.33	-2.26±0.42	0.025	-2.31	9.42±1.18	-2.29±0.99

Table 1 Measurements of drift from the baseline experiments in the JEOL 2100 calculated for DIC and PT drifting, along with the fitted parameters.

In order to obtain a better estimate of noise levels in these images small-angle rigid rotations are also considered as a contribution to the noise. To account for possible rigid rotation, we can analyze the results by fitting both a rotation and translation to the DIC results, using the following expressions:

$$u_i = A_1 y_i + A_2 \tag{5}$$

$$v_i = B_1 x_i + B_2 \tag{6}$$

where (x_i , y_i) are the coordinates of the i-th correlation point; A_1, B_1 represent rotation angles (in rad), and rigid translations are denoted by A_2, B_2. Note that in theory A_1 should equal B_1 since they should represent the same rigid rotation amount, although they can be measured independently by a least squares fitting to equation (5), (6) to the u and v measurements separately. Note also that the rigid translation portions are effectively equivalent to the average u_{DIC} *and* v_{DIC} values discussed above in Figs. 10 and 11. Table 1 shows the results of these fits for all cases for the JEOL microscope. Rotation angles are of the order $\leq 10^{-4}$, thus rigid translation is dominant, as is

also visible by eye in Fig. 9a or by comparing u_{DIC}, v_{DIC} to A_2, B_2 in Table 1. In-plane rigid rotations are anticipated to be small due to the geometry and loading configuration of the TEM specimen rod. The results of measured and fitted displacements for all cases studied here are also shown in Fig. 10 as the solid lines connecting the cross symbols. As is seen in Fig. 10, the average u_{DIC}, v_{DIC} are extremely close to the fitted translation measurements A_2, B_2, as is also confirmed in Table 1 for the JEOL microscope. Note that standard deviations of fitted results are at least 10 times smaller than those of averaged results, and thus are not visible in Fig. 10. By subtracting the average displacements from the quiver plot of Fig. 9a we obtain the results shown in Fig. 9b, where the residual displacement patterns now appear more random and much smaller in magnitude than the drift in all cases and for both camera/microscope combinations.

4.2 Deformation measurements

Fig. 11 shows DIC contour plots for both *u* and *v* displacements as marked for two instances of time: one at t = 20 s near the end of the ramp loading (see Fig. 6a) and one near the end of the creep portion of the loading at t = 296 s. The field of view of this image is approximately that shown in Fig. 4a and is centered around the midspan of the beam. From Fig. 11 we can observe that most of the sample region can be correlated. The few points that lose correlation, can be related either to an inappropriate size of the grown nanoparticles or a locally insufficient speckle pattern density. In addition, many points near the top edge of the sample fail to correlate due to edge effects in the pattern resulting from sample preparation.

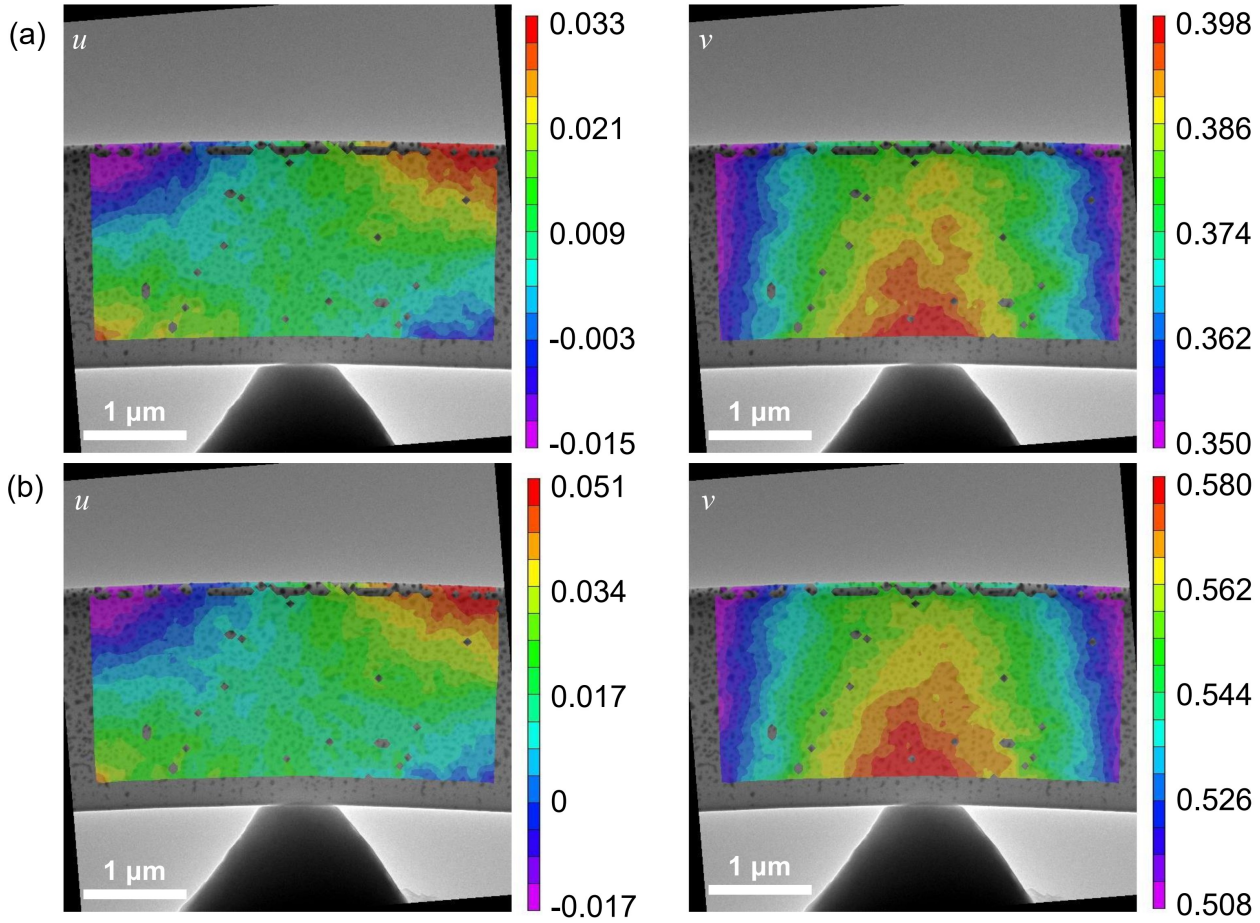

Fig. 11 DIC results for measurements of *u, v* displacement during in-situ loading at (a) t = 20 s; (b) t = 296 s. All values are in μm.

Fig. 8 illustrates selected particle tracking results obtained using Trackmate after filtering unrealistic trajectories that result from linking different particles together into a single track. This effect may be seen in some of the blue trajectories shown in Fig. 8. The pink circles represent particles detected in the first image and the colored lines are trajectories of particles as measured from a sequence of the 14 images. Particle tracking cannot provide a full-field displacement measurement in the sense of DIC, but it is possible to obtain local trajectories of several particles using PT. In this experiment, 368 particles were detected, a number which can be varied according

to the manually input threshold and estimated particle diameter. Of these, 356 (96.7%) trajectories considered unrealistic were filtered and excluded from the analysis. The large number of filtered trajectories results from the aforementioned issue that the experiment was not optimized for PT data collection. Ideally, the distance between particles within an image should be large relative to the linking distances between images. It should be feasible to improve number and density of particles tracked effectively by increasing the temporal resolution of the PT measurements and optimizing the pattern for PT [51]. It is desirable, nevertheless, to perform PT to the extent possible so that the data set can be compared to the DIC results.

4.3 Comparison between DIC and PT

Before comparing DIC and PT results over the entire deformation field, a validation of both methods is performed by comparing with the applied load point displacement that is also recorded by the far-field loading device (Fig. 6b). Since both DIC and PT provide measurements some distance away from the boundary of the specimen, DIC measurements are at the center of a subset and PT measurements are at a Feret point (i.e. the central position of a tracked particle), neither a DIC correlation point or a PT measurement point exists directly on the surface at the point of contact with the indenter. Additionally, DIC correlation points and PT measurements are not coincident at precisely the same locations throughout the entire sample. It would be possible to co-register these measurement points, and also include other specific points of interest such as points on the boundary, by performing any number of various interpolation schemes on the measured data. These may include transferring the data onto a finite element grid that may also enforce compatibility, or performing spline fitting and smoothing of the data, among others [52]. Such operations were avoided here in order to prevent introduction of additional errors or smoothing artifacts. As a proof-of-concept the closest *direct* measurement point available to the center of the

indenter from either DIC or PT are plotted as a function of time in Fig. 6b together with the far-field measurements. This effectively places the DIC and PT measurement points about 1 to 2 subsets, i.e. about 150 pixels, below the actual loading point. Note that since this experiment was performed in load control, the displacement measurements shown here are independent and can validate each other, although far-field displacement measured from the loading device also includes any compliance effects from the load cell and the sample gripping mechanism. Nonetheless, despite all the issues mentioned above, the agreement in Fig. 6b between these three independent measurements is very good and provides validation for both the DIC and PT measurements.

In Section 4.1 we discussed DIC "noise" estimates based on sample drift. Such sample drift, which essentially is a rigid motion of the object and not random noise, would also be detectable by PT applied to the baseline images. Fig. 12 compares the DIC and PT drifting results for the JEOL microscope system, i.e., the figure is a full-field equivalent of Fig. 10c for the JEOL TEM. As mentioned above, the DIC correlation points were not exactly co-registered with the PT measurement points. Rather correlation points in DIC that were closest to the position of detected particles in PT were selected for this plot. A measure, on this scale, of how far off the DIC correlation points are from the PT measurement locations is seen in the small differences of the starting points of the DIC and PT trajectories. Fig. 12 highlights how DIC and PT generally capture the same drifting level, but that for measurement of such small displacements, some differences between trajectories, representing noise, are visible. Measured drift displacements from DIC and PT are shown in Table 1. PT shows a larger standard deviation, ~1 nm, that indicates a fluctuation range of ~1 pixel, while DIC gives a fluctuation range that is much smaller than 1 pixel. This is consistent with the expectation that PT will not produce appreciable sub-pixel resolution.

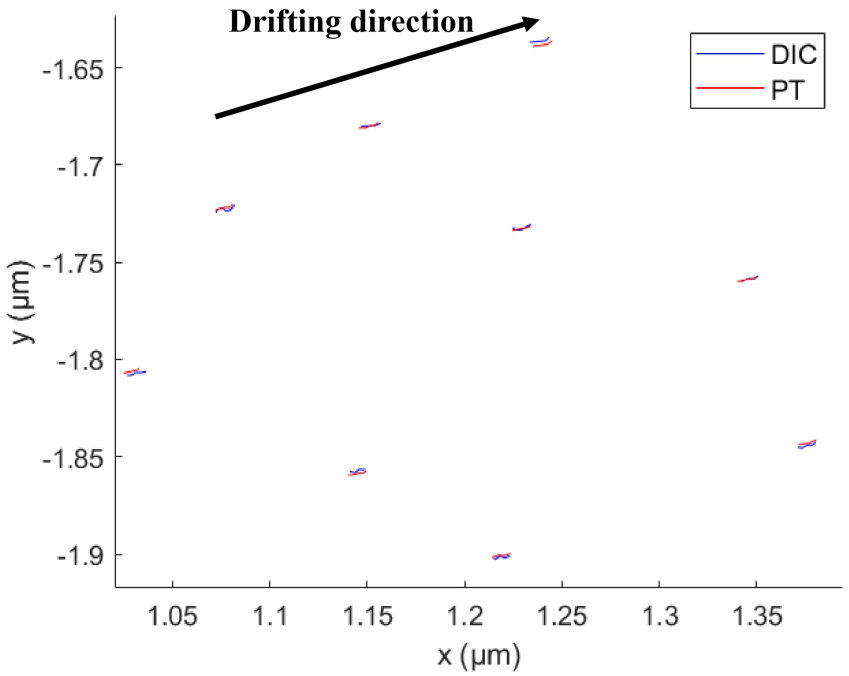

Fig. 12 Drifting displacement measured by DIC and PT.

Fig. 13 presents a direct comparison of DIC and PT trajectories during the ramp loading and creep phases of the experiment. The geometric center of the beam sample has been set as the origin in this figure. Selected positions of correlation points/detected particles are then connected with a color scheme of the lines denoting time evolution from 0 s to 300 s, recall that ramp loading ended at 23 s and the load was constant thereafter. As before the small difference from not co-registering the DIC and PT measurement points is visible by the small shift of the starting point of each trajectory. Nonetheless, Fig. 13 shows that DIC and PT results match well since discrete points for DIC and PT are coincident, hence providing corroborative evidence of feasibility for both DIC and PT measurements. The color bar denoting the time evolution highlights the fact that both DIC and PT give comparable results for most trajectories both in terms of magnitude and temporal evolution. There are, however, some trajectories which exhibit discrepancies, mostly near the sample's edges.

For example, for the black-circled trajectory near the top of the beam, 5 images (frame 4, 5, 10, 12, 14) could not be correlated in DIC, as is illustrated in the time sequence of displacements from this specific location shown in the central inset of Fig. 13. Exported displacement data for an uncorrelated point in one image maintains the same value of the previous image, see plateaus in red curve in central inset in Fig. 13. To "supplement" these missing DIC results, an alternate strategy is to conduct incremental correlation, i.e., correlate an image with the immediately previous image rather than with the first/reference undeformed image. The result of such an incremental correlation is also shown in the inset plot as the green curve, which compares very well to the displacement history measured by PT at the corresponding location. Another example trajectory is shown in the red-circled location where we can see an initially good agreement between DIC and PT measurements become divergent because of errors in the PT trajectory measurement. Overall, however, the agreement between the two methods is very good. Therefore, despite occasional issues with effectiveness of DIC or PT locally, which to some extent might be overcome by incremental DIC or by filtering incorrect trajectories in PT, the accuracy of both measurements is at or below the length scale of a pixel providing nanometer and sub-nanometer measurements of displacement.

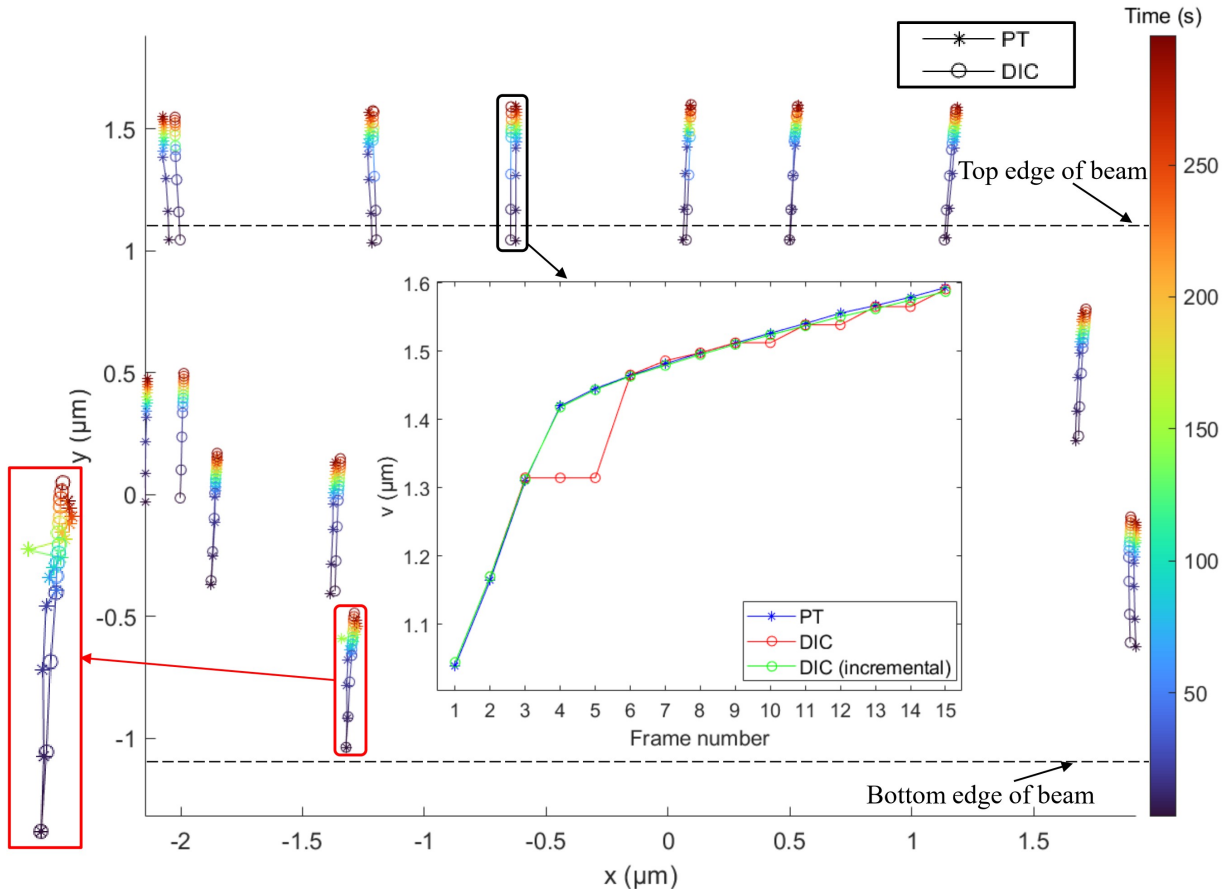

Fig. 13 Displacement results from DIC and PT applied to in-situ loading of a microscale amorphous SiO2 beam. The inset shows the evolution of the highlighted data and demonstrates how uncorrelated points in the DIC calculated using regular correlation may be fixed using incremental correlation. The time between frames is ≈ 7 s at ramp loading and 25 s at constant load stage.

5. Conclusions

The previous sections discussed *in situ* microscale displacement measurement of amorphous SiO_2 loaded *in situ* in the TEM using Digital Image Correlation (DIC) and Particle Tracking (PT) techniques. The conclusions of this work are the following:

a) Gold nanoparticles formed via thermally induced thin film de-wetting can serve as both effective speckle patterns for DIC and as particles for PT in the TEM.

b) DIC and PT provide highly comparable full-field displacement measurements, demonstrating the effectiveness of both methods. Measurements can contain noise and imaging drifting artifacts, which can be microscope and camera dependent. For the microscope systems of interest here, a JEOL and a Hitachi, we measured drift rates of 7.88×10^{-5} μm/s and 3.17×10^{-5} μm/s, respectively.

c) For amorphous materials, DIC and PT are both applicable for displacement measurements in the TEM. Nonetheless, the feasibility of applying these methods to crystalline materials needs further exploration. As an initial speculation, DIC is more likely to encounter difficulties when applied to crystalline materials due to diffraction effects in the image intensity. These problems might be circumvented by employing an incoherent scattering technique such as high-angle annular dark-field scanning transmission electron microscopy, but this would introduce common errors associated with scanning artifacts. PT, however, should be less sensitive to small variations in local intensity resulting from small changes in diffraction condition, but might also be sensitive to errors when imaged near strong diffraction conditions. Future efforts will include applying these methods to crystalline materials, extracting material properties from such experimental measurements, and developing microscale mechanical models that can illustrate and/or predict material behavior based on this work.

Acknowledgements

This work was carried out in the Materials Research Laboratory Central Research Facilities, University of Illinois. Funding for this research was provided by the National Science Foundation (grant No. CMMI 18-25466). The authors acknowledge Dr. Waclaw Swiech and Dr. Changqiang Chen for help with TEM and Picoindenter experiments. LF also acknowledges funding from National Natural Science Foundation of China (Grant No. 51902351) and Natural Science Foundation of Guangdong Province, China (Grant No. 20191515010693).

Data Availability

The raw/processed data required to reproduce these findings cannot be shared at this time as the data also forms part of an ongoing study.

References

[1] Z. Shan, J.A. Knapp, D.M. Follstaedt, E.A. Stach, J.M.K. Wiezorek, S.X. Mao, Inter- and intra-agglomerate fracture in nanocrystalline nickel., Phys. Rev. Lett. 100 (2008) 105502. https://doi.org/10.1103/PhysRevLett.100.105502.

[2] Q. Yu, Z.-W. Shan, J. Li, X. Huang, L. Xiao, J. Sun, E. Ma, Strong crystal size effect on deformation twinning., Nature. 463 (2010) 335–338. https://doi.org/10.1038/nature08692.

[3] Z.W. Shan, J. Li, Y.Q. Cheng, A.M. Minor, S.A. Syed Asif, O.L. Warren, E. Ma, Plastic flow and failure resistance of metallic glass: Insight from in situ compression of nanopillars, Phys. Rev. B. 77 (2008) 155419. https://doi.org/10.1103/PhysRevB.77.155419.

[4] Q. Deng, Y. Cheng, Y. Yue, L. Zhang, Z. Zhang, X. Han, E. Ma, Uniform tensile elongation in framed submicron metallic glass specimen in the limit of suppressed shear banding, Acta Mater. 59 (2011) 6511–6518. https://doi.org/10.1016/j.actamat.2011.05.035.

[5] A.M. Minor, S.A.S. Asif, Z. Shan, E.A. Stach, E. Cyrankowski, T.J. Wyrobek, O.L. Warren, A new view of the onset of plasticity during the nanoindentation of aluminium., Nat. Mater. 5 (2006) 697–702. https://doi.org/10.1038/nmat1714.

[6] K. Zheng, C. Wang, Y.-Q. Cheng, Y. Yue, X. Han, Z. Zhang, Z. Shan, S.X. Mao, M. Ye, Y. Yin, E. Ma, Electron-beam-assisted superplastic shaping of nanoscale amorphous silica., Nat. Commun. 1 (2010) 24. https://doi.org/10.1038/ncomms1021.

[7] Y. Zou, P. Okle, H. Yu, T. Sumigawa, T. Kitamura, S. Maiti, W. Steurer, R. Spolenak, Fracture properties of a refractory high-entropy alloy: In situ micro-cantilever and atom probe tomography studies, Scr. Mater. 128 (2017) 95–99. https://doi.org/10.1016/j.scriptamat.2016.09.036.

[8] R. Gauvin, Review of transmission electron microscopy for the characterization of materials, in: Materials Characterization and Optical Probe Techniques: A Critical Review, SPIE, 1997: p. 102910C. https://doi.org/10.1117/12.279840.

[9] M.A. Haque, M.T.A. Saif, Application of MEMS force sensors for in situ mechanical characterization of nano-scale thin films in SEM and TEM, Sensors and Actuators A: Physical. 97–98 (2002) 239–245. https://doi.org/10.1016/S0924-4247(01)00861-5.

[10] D. Kiener, A.M. Minor, Source truncation and exhaustion: insights from quantitative in situ TEM tensile testing., Nano Lett. 11 (2011) 3816–3820. https://doi.org/10.1021/nl201890s.

[11] Z. Shan, In situ TEM investigation of the mechanical behavior of micronanoscaled metal pillars, JOM. 64 (2012) 1229–1234. https://doi.org/10.1007/s11837-012-0436-8.

[12] L. Feng, R. Hao, J. Lambros, S.J. Dillon, The influence of dopants and complexion transitions on grain boundary fracture in alumina, Acta Mater. 142 (2018) 121–130. https://doi.org/10.1016/j.actamat.2017.09.002.

[13] E. Hosseinian, O.N. Pierron, Quantitative in situ TEM tensile fatigue testing on nanocrystalline metallic ultrathin films., Nanoscale. 5 (2013) 12532–12541. https://doi.org/10.1039/c3nr04035f.

[14] J.R. Greer, W.D. Nix, Size dependence of mechanical properties of gold at the sub-micron scale, Appl. Phys. A. 80 (2005) 1625–1629. https://doi.org/10.1007/s00339-005-3204-6.

[15] Q. Yu, J. Kacher, C. Gammer, R. Traylor, A. Samanta, Z. Yang, A.M. Minor, In situ TEM observation of FCC Ti formation at elevated temperatures, Scr. Mater. 140 (2017) 9–12. https://doi.org/10.1016/j.scriptamat.2017.06.033.

[16] W.H. Peters, Digital Imaging Techniques In Experimental Stress Analysis, Opt. Eng. 21 (1982) 213427. https://doi.org/10.1117/12.7972925.

[17] M.A. Sutton, W.J. Wolters, W.H. Peters, W.F. Ranson, S.R. McNeill, Determination of displacements using an improved digital correlation method, Image Vis. Comput. 1 (1983) 133–139. https://doi.org/10.1016/0262-8856(83)90064-1.

[18] J.-N. Périé, S. Calloch, C. Cluzel, F. Hild, Analysis of a multiaxial test on a C/C composite by using digital image correlation and a damage model, Exp. Mech. 42 (2002) 318–328. https://doi.org/10.1007/BF02410989.

[19] J.M. Considine, C.T. Scott, R. Gleisner, J.Y. Zhu, Use of digital image correlation to study the local deformation field of paper and paperboard, Proceedings of the Advances in Paper Science and Technology : 13th Fundamental Research Symposium, 2005 September 11-16, Cambridge, UK. Cambridge, UK : The Pulp and Paper Fundamental Research Society, 2005: Pages 613-630. (2005).

[20] Z. Sun, J.S. Lyons, S.R. McNeill, Measuring Microscopic Deformations with Digital Image Correlation, Opt. Lasers Eng. 27 (1997) 409–428. https://doi.org/10.1016/S0143-8166(96)00041-3.

[21] R. Ambu, F. Aymerich, F. Bertolino, Investigation of the effect of damage on the strength of notched composite laminates by digital image correlation, The Journal of Strain Analysis for Engineering Design. 40 (2005) 451–461. https://doi.org/10.1243/030932405X16106.

[22] N. Sabaté, D. Vogel, A. Gollhardt, J. Keller, B. Michel, C. Cané, I. Gràcia, J.R. Morante, Measurement of residual stresses in micromachined structures in a microregion, Appl. Phys. Lett. 88 (2006) 071910. https://doi.org/10.1063/1.2177357.

[23] F. Lagattu, F. Bridier, P. Villechaise, J. Brillaud, In-plane strain measurements on a microscopic scale by coupling digital image correlation and an in situ SEM technique, Materials Characterization. 56 (2006) 10–18. https://doi.org/10.1016/j.matchar.2005.08.004.

[24] M.A. Sutton, N. Li, D.C. Joy, A.P. Reynolds, X. Li, Scanning Electron Microscopy for Quantitative Small and Large Deformation Measurements Part I: SEM Imaging at Magnifications from 200 to 10,000, Exp. Mech. 47 (2007) 775–787. https://doi.org/10.1007/s11340-007-9042-z.

[25] X.G. Wang, C.H. Liu, B.B. He, C. Jiang, M.X. Huang, Microscopic strain partitioning in Lüders band of an ultrafine-grained medium Mn steel, Materials Science and Engineering: A. 761 (2019) 138050. https://doi.org/10.1016/j.msea.2019.138050.

[26] C.C. Tasan, J.P.M. Hoefnagels, M.G.D. Geers, Microstructural banding effects clarified through micrographic digital image correlation, Scr. Mater. 62 (2010) 835–838. https://doi.org/10.1016/j.scriptamat.2010.02.014.

[27] M.D. McMurtrey, G.S. Was, B. Cui, I. Robertson, L. Smith, D. Farkas, Strain localization at dislocation channel–grain boundary intersections in irradiated stainless steel, International Journal of Plasticity. 56 (2014) 219–231. https://doi.org/10.1016/j.ijplas.2014.01.001.

[28] A.D. Kammers, S. Daly, Digital Image Correlation under Scanning Electron Microscopy: Methodology and Validation, Exp. Mech. 53 (2013) 1743–1761. https://doi.org/10.1007/s11340-013-9782-x.

[29] G. Vendroux, W.G. Knauss, Submicron deformation field measurements: Part 1. Developing a digital scanning tunneling microscope, Exp. Mech. 38 (1998) 18–23. https://doi.org/10.1007/BF02321262.

[30] S. Cho, I. Chasiotis, T.A. Friedmann, J.P. Sullivan, Young's modulus, Poisson's ratio and failure properties of tetrahedral amorphous diamond-like carbon for MEMS devices, J. Micromech. Microeng. 15 (2005) 728–735. https://doi.org/10.1088/0960-1317/15/4/009.

[31] X. Wang, Z. Pan, F. Fan, J. Wang, Y. Liu, S.X. Mao, T. Zhu, S. Xia, Nanoscale Deformation Analysis With High-Resolution Transmission Electron Microscopy and Digital Image Correlation, J. Appl. Mech. 82 (2015) 121001. https://doi.org/10.1115/1.4031332.

[32] V. Valle, S. Hedan, P. Cosenza, A.L. Fauchille, M. Berdjane, Digital image correlation development for the study of materials including multiple crossing cracks, Exp. Mech. 55 (2015) 379–391. https://doi.org/10.1007/s11340-014-9948-1.

[33] F. Bourdin, J.C. Stinville, M.P. Echlin, P.G. Callahan, W.C. Lenthe, C.J. Torbet, D. Texier, F. Bridier, J. Cormier, P. Villechaise, T.M. Pollock, V. Valle, Measurements of plastic localization by heaviside-digital image correlation, Acta Mater. 157 (2018) 307–325. https://doi.org/10.1016/j.actamat.2018.07.013.

[34] Y. Ososkov, D.S. Wilkinson, M. Jain, T. Simpson, In-situ measurement of local strain partitioning in a commercial dual-phase steel, IJMR. 98 (2007) 664–673. https://doi.org/10.3139/146.101526.

[35] Y. Tanaka, K. Naito, S. Kishimoto, Y. Kagawa, Development of a pattern to measure multiscale deformation and strain distribution via in situ FE-SEM observations., Nanotechnology. 22 (2011) 115704. https://doi.org/10.1088/0957-4484/22/11/115704.

[36] D. Grégoire, O. Loh, A. Juster, H.D. Espinosa, In-situ AFM Experiments with Discontinuous DIC Applied to Damage Identification in Biomaterials, Exp. Mech. 51 (2011) 591–607. https://doi.org/10.1007/s11340-011-9463-6.

[37] A.D. Kammers, S. Daly, Self-Assembled Nanoparticle Surface Patterning for Improved Digital Image Correlation in a Scanning Electron Microscope, Exp. Mech. 53 (2013) 1333–1341. https://doi.org/10.1007/s11340-013-9734-5.

[38] J.P.M. Hoefnagels, M.P.F.H.L. van Maris, T. Vermeij, One-step deposition of nano-to-micron-scalable, high-quality digital image correlation patterns for high-strain in-situ multi-microscopy testing, Strain. 55 (2019) e12330. https://doi.org/10.1111/str.12330.

[39] S. Shafqat, J.P.M. Hoefnagels, Cool, Dry, Nano-scale DIC Patterning of Delicate, Heterogeneous, Non-planar Specimens by Micro-mist Nebulization, Exp. Mech. (2021). https://doi.org/10.1007/s11340-020-00686-2.

[40] S.-H. Joo, J.K. Lee, J.-M. Koo, S. Lee, D.-W. Suh, H.S. Kim, Method for measuring nanoscale local strain in a dual phase steel using digital image correlation with nanodot patterns, Scr. Mater. 68 (2013) 245–248. https://doi.org/10.1016/j.scriptamat.2012.10.025.

[41] G. Seguini, J.L. Curi, S. Spiga, G. Tallarida, C. Wiemer, M. Perego, Solid-state dewetting of ultra-thin Au films on SiO_2 and HfO_2., Nanotechnology. 25 (2014) 495603. https://doi.org/10.1088/0957-4484/25/49/495603.

[42] F. Leroy, Ł. Borowik, F. Cheynis, Y. Almadori, S. Curiotto, M. Trautmann, J.C. Barbé, P. Müller, How to control solid state dewetting: A short review, Surf. Sci. Rep. 71 (2016) 391–409. https://doi.org/10.1016/j.surfrep.2016.03.002.

[43] W. Primak, Stress relaxation of vitreous silica on irradiation, J. Appl. Phys. 53 (1982) 7331–7342. https://doi.org/10.1063/1.330141.

[44] S. Özerinç, H.J. Kim, R.S. Averback, W.P. King, Direct measurements of irradiation-induced creep in micropillars of amorphous $Cu_{56}Ti_{38}Ag_6$, $Zr_{52}Ni_{48}$, Si, and SiO_2, J. Appl. Phys. 117 (2015) 024310. https://doi.org/10.1063/1.4905019.

[45] M.A. Sutton, J.-J. Orteu, H.W. Schreier, Digital image correlation (DIC), in: Image Correlation for Shape, Motion and Deformation Measurements, Springer US, Boston, MA, 2009: pp. 1–37. https://doi.org/10.1007/978-0-387-78747-3_5.

[46] J.-Y. Tinevez, N. Perry, J. Schindelin, G.M. Hoopes, G.D. Reynolds, E. Laplantine, S.Y. Bednarek, S.L. Shorte, K.W. Eliceiri, TrackMate: An open and extensible platform for single-particle tracking., Methods. 115 (2017) 80–90. https://doi.org/10.1016/j.ymeth.2016.09.016.

[47] J. Schindelin, I. Arganda-Carreras, E. Frise, V. Kaynig, M. Longair, T. Pietzsch, S. Preibisch, C. Rueden, S. Saalfeld, B. Schmid, J.-Y. Tinevez, D.J. White, V. Hartenstein, K. Eliceiri, P. Tomancak, A. Cardona, Fiji: an open-source platform for biological-image analysis., Nat. Methods. 9 (2012) 676–682. https://doi.org/10.1038/nmeth.2019.

[48] T. Lindeberg, Feature Detection with Automatic Scale Selection, Springer Science and Business Media LLC. (1998). https://doi.org/10.1023/a:1008045108935.

[49] K. Jaqaman, D. Loerke, M. Mettlen, H. Kuwata, S. Grinstein, S.L. Schmid, G. Danuser, Robust single-particle tracking in live-cell time-lapse sequences., Nat. Methods. 5 (2008) 695–702. https://doi.org/10.1038/nmeth.1237.

[50] J. Munkres, Algorithms for the Assignment and Transportation Problems, Journal of the Society for Industrial and Applied Mathematics. 5 (1957) 32–38.

[51] Y. Kerkhoff, S. Block, Analysis and refinement of 2D single-particle tracking experiments., Biointerphases. 15 (2020) 021201. https://doi.org/10.1116/1.5140087.

[52] B. Wang, B. Pan, Subset-based local vs. finite element-based global digital image correlation: A comparison study, Theor. Appl. Mech. Lett. 6 (2016) 200–208. https://doi.org/10.1016/j.taml.2016.08.003.